

Negative stiffness and enhanced damping of individual multiwalled carbon nanotubes

H. W. Yap,¹ R. S. Lakes,³ and R. W. Carpick^{2,*}

¹*Department of Physics, University of Pennsylvania, Philadelphia, Pennsylvania 19104, USA*

²*Department of Mechanical Engineering and Applied Mechanics, University of Pennsylvania, Philadelphia, Pennsylvania 19104, USA*

³*Department of Engineering Physics, University of Wisconsin-Madison, Madison, Wisconsin 53706, USA*

(Received 4 October 2007; published 24 January 2008)

The mechanical instabilities and viscoelastic response of individual multiwalled carbon nanotubes and nanofibers (MWCNTs/Fs) under uniaxial compression are studied with atomic force microscopy. Specific buckling events are evident by regimes of negative stiffness, i.e., marked drops in force with increasing compression. Uniaxial cyclic loading can be repeatedly executed even in initially postbuckled regimes, where the CNTs/Fs display incremental negative stiffness. Increases in mechanical damping of 145–600 % in these initially postbuckled regimes, as compared to the linear prebuckled regimes, are observed. Increased damping is attributed to frictional energy dissipation of walls in buckled configurations of the MWCNTs/Fs. This represents the extension of the concept of negative stiffness to the scale of nanostructures and opens up possibilities for designing nanocomposites with high stiffness and high damping simultaneously.

DOI: [10.1103/PhysRevB.77.045423](https://doi.org/10.1103/PhysRevB.77.045423)

PACS number(s): 62.25.-g, 62.40.+i, 61.46.Fg

I. INTRODUCTION

The concept of using mechanical elements with negative stiffness has recently been established as a novel paradigm for designing structural and mechanical systems.^{1–4} Negative structural stiffness involves a reversal of the usual positive relation between force and displacement in a deformed structure or material. One consequence of negative stiffness is the possibility of enhanced overall stiffness and damping of a composite system with negative stiffness inclusions. These can be achieved if the inclusions are stabilized within a positive stiffness matrix.¹ For example, a small fraction of negative shear modulus inclusions of ferroelastic vanadium dioxide in a pure tin matrix resulted in extreme mechanical damping and anomalies in stiffness. Under certain temperature ranges, these negative shear modulus inclusions are more effective than diamond inclusions in increasing the overall composite stiffness.² These increases in stiffness have also been witnessed in composites with negative bulk modulus inclusions of barium titanate in a tin matrix, whose overall incremental Young's moduli exceeded that of diamond.³ Lakes⁴ has also shown that simple macroscopic rubber tubes exhibit negative incremental stiffness and enhanced damping when they kink (i.e., exhibiting asymmetric shell buckling) under uniaxial compression. Another example of a mechanical instability that leads to negative incremental stiffness is in compression and subsequent symmetric shell buckling of circular thin cylindrical shells.⁵

In general, carbon nanotubes and nanofibers (CNTs/Fs) exhibit an excellent mechanical behavior derived from the extremely high stiffness of the C–C atomic bonds,⁶ including reversibility even under large deformations.⁷ This suggests that CNTs/Fs should be able to exhibit a pronounced and fully reversible negative stiffness behavior. Using molecular dynamics (MD) and finite element simulations, respectively, both Jakobson *et al.*⁸ and Pantano *et al.*⁹ predicted a regime of negative incremental stiffness in the initially postbuckled regime of uniaxially compressed single walled CNTs. The MD simulations of Garg *et al.*¹⁰ also predicted a drop in

force due to the elastic kink deformations for CNTs indented on stiff surfaces. Negative incremental stiffness, as evidenced by reversible drops in force versus displacement curves, has been experimentally observed and quantified in terms of buckling mechanics in axially compressed multiwalled carbon nanotubes and nanofibers (MWCNTs/Fs) by Yap *et al.*¹¹

The use of CNT negative stiffness to enhance damping in composites has not yet been demonstrated. Polymer nanocomposites fabricated with CNT inclusions have been shown to exhibit increased damping.^{12–16} However, these gains in damping are achieved within the elastically deformed, prebuckled regime of the CNT inclusions. The increased damping is attributed to interfacial friction damping and corresponding energy dissipation at either CNT-polymer interfaces or CNT-CNT interfaces. Here, we report dramatically increased mechanical damping of mechanical systems comprised of atomic force microscopy (AFM) cantilever probes and an individual MWCNT/F in the initially postbuckled negative stiffness regime during controlled cyclic axial loading.

II. EXPERIMENTAL SECTION

Two types of AFM cantilever–MWCNT/F configurations are used in this initial study [Fig. 1(a)]. One involves the MWCNT affixed directly to an AFM tip (scheme I). The other involves the AFM tip brought into direct contact with a vertically aligned MWCNT/F fixed at one end by a nanopore in a substrate (scheme II). Both configurations correspond crudely to the Reuss composite (series) structure (scheme R), which involves planar layers aligned transversely to the direction of the applied load so that each component experiences the same stress.⁴ In these configurations, the substrates and, more importantly, the AFM cantilevers act as stabilizing and constraining positive stiffness components.

The MWCNTs in scheme I have aspect ratios ranging from 80 to 220. Their average diameter and wall thickness, based on transmission electron microscope (TEM) measure-

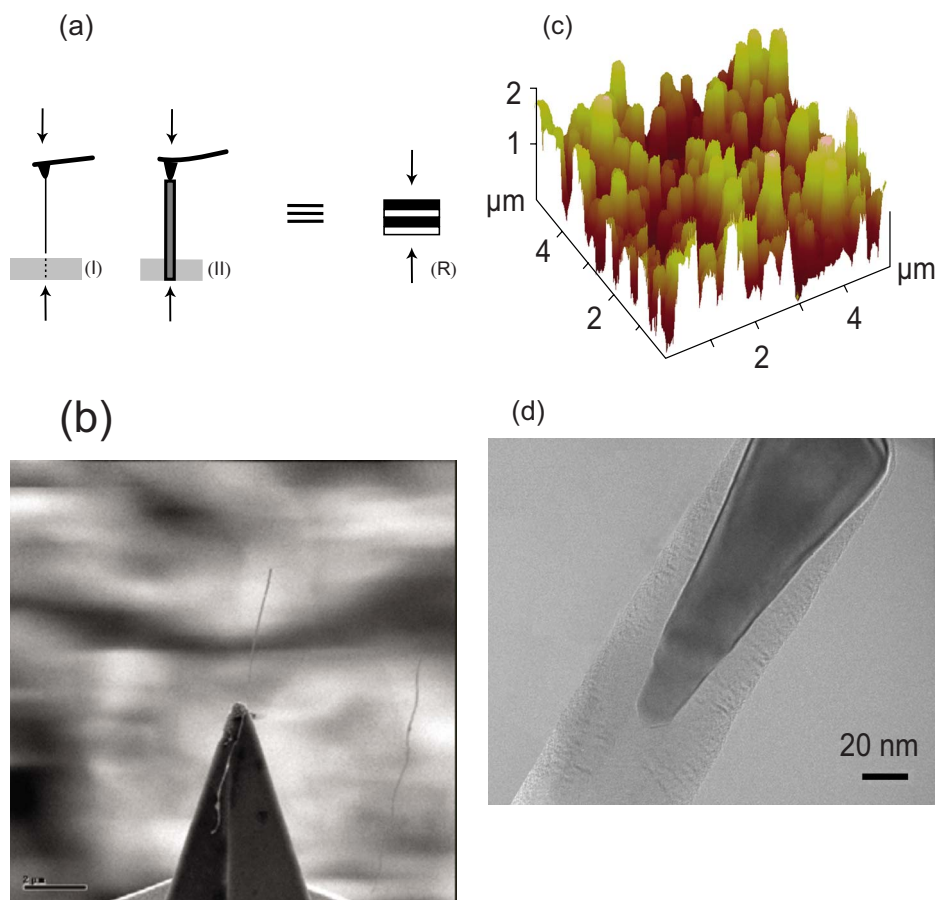


FIG. 1. (Color online) (a) AFM-MWCNT configurations (schemes I and II) used in this study, resembling qualitatively the Reuss (series) composite (scheme R) model. Scheme I: AFM tip-mounted MWCNT configuration. Scheme II: AFM tip on AAO-grown MWCNT/F configuration. (b) SEM image of an AFM tip-mounted MWCNT. (c) AFM topographic image of the vertically aligned MWCNTs/Fs grown from AAO pores. (d) TEM image of one of these MWCNTs/Fs, showing a thick wall structure and the nickel catalyst at the tip.

ments of ten different tubes, are 30 and 10 nm, respectively. The latter corresponds to approximately an average of 30 walls. Based on the TEM studies, the defect concentration is minimal,¹⁷ and there are few signs of initial damage or kinks. As discussed previously, they exhibit Euler and asymmetric shell buckling (kinking) upon axial compression.¹¹ In the case of scheme II, the MWCNTs/Fs have aspect ratios of 18–45, with the average at 35 (average length of 1.44 μm). Their average diameter and wall thickness are 86 and 31 nm, respectively. The latter translates to approximately 91 walls. These numbers are based on TEM measurements of 30 MWCNTs/Fs. As discussed elsewhere, for the MWCNFs, the average angle of the walls with respect to the main axis is small, i.e., $\sim 7^\circ$, and they exhibit more defects than the MWCNTs. Some of the MWCNFs also exhibit herringbone-like defects. Overall, both of them are less pristine than the MWCNTs of scheme I. At times, these MWCNTs/Fs exhibit symmetric shell buckling.¹¹

Figure 1(b) is a scanning electron microscope (SEM) image of a contact mode AFM tip-mounted MWCNT¹⁷ used in scheme I. Figure 1(c) is an AFM topographic image of free-standing, vertically aligned MWCNTs/Fs grown out of an anodized aluminum oxide (AAO) pore membrane used for scheme II. More details of the growth are presented by Yap

et al.^{11,18} Briefly, the AAO membrane provides a fixed mechanical boundary condition for the MWCNTs/Fs, and the pore spacing ensures that the MWCNTs/Fs are separated and thus noninteracting. Figure 1(d) is a TEM image of one of the MWCNTs/Fs from this sample, demonstrating the high growth quality.

III. RESULTS AND DISCUSSION

Figure 2(a) shows a representative force versus relative sample displacement (and strain) plot of the axial compression of a moderate aspect ratio MWCNT (length=1.2 μm , diameter=30 nm) attached to an AFM tip [similar to the one shown in Fig. 1(d)]. A linear increase in force at the beginning of loading is followed by a negative stiffness region, indicating the formation of a kink in the structure.¹¹ The inset of Fig. 2(a) shows the force plots at two different times (75 cycles apart; the frequency of cycles is 1 Hz). The difference between their overall features is minimal (later a red plot is adjusted downward for clarity). Figure 2(b) is a representative force versus relative sample displacement (strain) curve of the axial compression of a MWCNT/F grown from the AAO pores (length=1.6 μm , average diameter=86 nm). The linear increase in force when MWCNT/F comes into

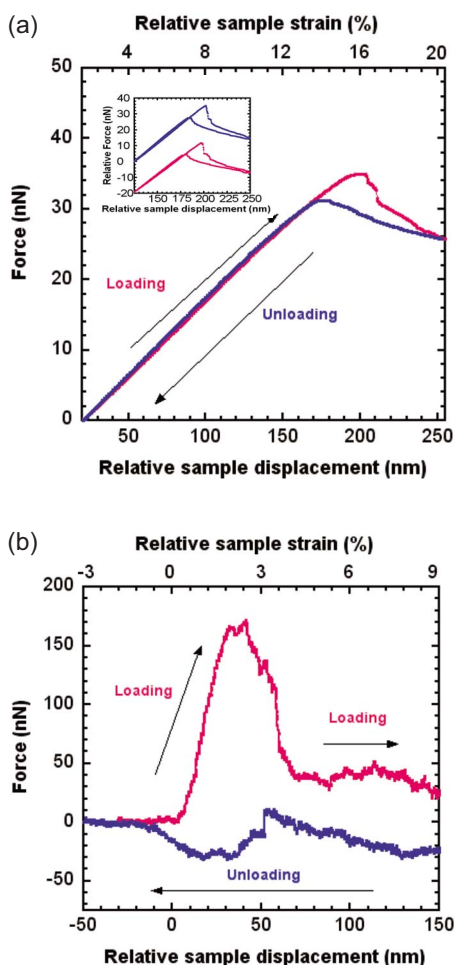


FIG. 2. (Color online) AFM Axial force versus relative vertical sample displacement and strain. (a) On an AFM tip-mounted MWCNT. (b) On an AAO-grown MWCNT/F. All tests were performed cyclically to large displacements multiple times at room temperature and at 1–2 Hz.

contact with the tip is followed by a sudden drop in force to a low but nonzero value. The transition of the slope is a signature of shell buckling, as described in detail previously.¹¹ For the above MWCNTs used and others, the loading characteristics are highly reversible for up to hundreds of cycles, as shown in the inset to Fig. 2(a). No plastic or other permanent local deformations of these MWCNT/Fs are observed in SEM images of the regions probed by the AFM. Uniaxial cyclic loading at small amplitudes (<50 nm) at different average values of compression were then performed using the AFM in both prebuckled and initial postbuckled regions. A Veeco (Digital Instruments) Multimode AFM with a Nanoscope IV controller was used for these experiments. Experiments were conducted in laboratory air at room temperature. A sine wave signal (0.8–1.2 Hz, below any resonance of the AFM) with a dc offset is used to drive the system (cantilever and nanotube) in the *z* direction. This is generated using an Agilent Technologies 33120A wave form/function generator. An operational amplifier is used to amplify this signal. The amplitude of oscillation applied to the sample is controlled with both the

function generator and the amplifier, while the predeformation or offset is mainly controlled by the amplifier’s dc offset feature. This generated sine wave signal is fed into the signal access module of the AFM. This is activated to drive the *z* piezo once a buckling phenomenon exhibiting negative stiffness is observed in the AFM’s conventional force mode. The regions of interest, i.e., prebuckled and initial postbuckled regimes, are then observed by reducing the amplitude of oscillation at the appropriate dc offset. Both this sine wave signal and the subsequent tip deflection signal are recorded continuously in the AFM and then plotted together, forming elliptical Lissajous figures. With these Lissajous figures, linear viscoelastic principles are applied to obtain viscoelastic properties. Occasionally, the buckling signatures for the AAO-grown MWCNTs/Fs fade away. This is due to thermal drifts of the stage. In such cases, repositioning or relocating the MWCNT/F is required. In order to characterize the viscoelastic properties of these configurations, the linearized complex moduli are calculated using the measured dynamic stress or force and its corresponding strain response. The linearized complex modulus of the overall configuration is given by $E^* = E' + iE'' = E'(1 + i \tan \delta)$, where $E' = \text{Re}(E^*)$ is the in-phase component of the overall modulus (storage modulus), $E'' = \text{Im}(E^*)$ is the out-of-phase component of the overall modulus (loss modulus), and δ is the phase angle ($\tan \delta$ is the loss tangent) between the stress and strain sinusoids.^{4,19}

Figure 3 shows the small-amplitude axial cyclic force versus the relative sample displacement *d* for the above AFM tip-mounted MWCNT configuration in (a) the prebuckled positive stiffness regime ($d_{av} \sim 75$ nm) and (b) the initial postbuckled negative stiffness regime ($d_{av} \sim 227$ nm). The displacement was cycled at 1.16 Hz.²⁰ The average sample displacement d_{av} is the position of the center of the controlled oscillation. The strain amplitudes in both cases are $\sim 3\%$. The purple lines are curve fits to the data. The curve fits are done using the KALEIDAGRAPH software. A general equation for an ellipse is used for the fits, with the fitting parameter as δ , the phase angle. From the curve fit results, we are able to obtain an absolute error in δ . Using the propagation of errors, we can determine the absolute error for the function $\tan \delta$. This turns out to be mostly a small percentage of the actual value itself. The modulus times area is actually dependent on observational parameters such as the force, the length of the MWCNT/F, and the relative sample displacement. It turns out that the absolute errors in moduli times areas are dependent largely on the terms containing the absolute errors in forces and lengths of the MWCNTs/Fs. The relative error in the force or force calibration has been estimated in our previous publication (Ref. 11). From there, we can determine the absolute errors in forces. As for the lengths of the MWCNTs/Fs, we estimate the absolute errors to be in the order of 100 nm based on TEM measurements of the AFM-tipped MWCNTs and AFM height profiles of the AAO-grown MWCNTs/Fs. Lastly, the absolute errors in the energy dissipated per cycle are dependent on terms containing the absolute errors in relative sample displacements and forces. The former are very small and the latter have already been addressed above. In all, the relative errors in energy dissipation per cycle are small. The hysteretic area enclosed

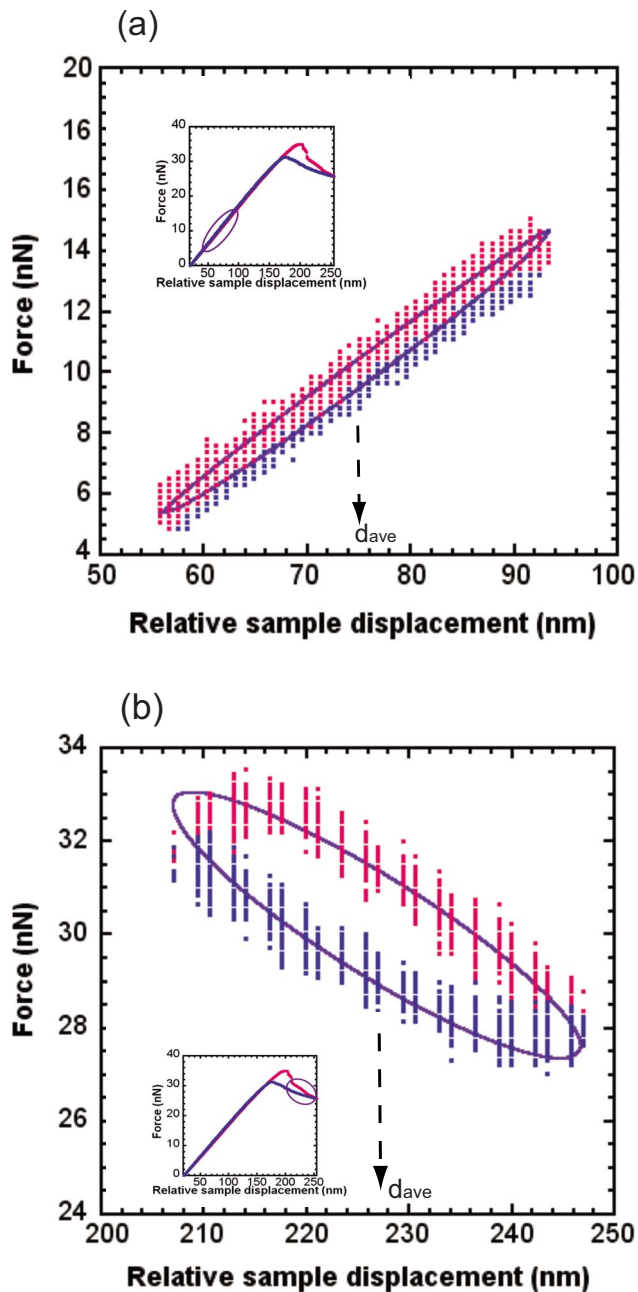


FIG. 3. (Color online) Higher resolution and magnification of cyclic axial loading for scheme II. (a) In the prebuckled regime, the CNT exhibits positive stiffness and the energy dissipation is minimal (negligible hysteresis). (b) In the initial postbuckled, the CNT exhibits negative stiffness regime and the energy dissipation is considerable (large hysteresis). All controlled cyclic loadings were performed within linear regimes, at ~ 1 Hz. Purple lines are least-squares curve fits to the raw data points. The insets identify the location of these controlled oscillations with respect to the force-displacement characteristics of Fig. 2(a). The mean displacement d_{av} is ~ 75 nm for (a) and ~ 227 nm for (b).

by the loop is proportional to the energy dissipation per cycle¹⁹ and is clearly larger in the initial postbuckled regime. Insets in both Figs. 3(a) and 3(b) show more precisely where these small oscillations are located in the force plots of Fig.

2(a). Any damping or hysteresis of the z motion of the piezo itself is small compared to that of the MWCNTs. This is verified by pressing an AFM cantilever on a stiff, nonlossy, atomically smooth surface (single crystal silicon) and by monitoring the force-deflection response of the cantilever. There is no observable phase difference for the same scales of force or displacement, thus demonstrating that neither the piezo nor the rest of the AFM system has any appreciable hysteresis for these scales. Part of the reason for this is that the piezo used for the z motion in this AFM is deliberately made of a “hard” piezo material that is chosen to have low hysteresis. In addition, hysteresis is minimal since we use small amplitudes and relatively low cycling frequencies. Also, the hysteresis of the piezo, if any, would appear equally in both the MWCNTs’ prebuckled and postbuckled stages of the study. However, it is clear that there is very little hysteresis in the prebuckled regime. According to bounding theorems on restrictions upon viscoelastic behavior,⁴ if one assumes a system with both non-negative stored energy and energy dissipation rate, then $E' \geq 0$. Here and in our subsequent experiments, there is stored energy (prestrain energy) in the system prior to the initial postbuckled regime. Thus, a negative E' in the initial postbuckled regime is not contradictory to these theorems. The behavior qualitatively follows the results of Lakes⁴ for macroscopic buckled tubes rather well.

Figure 4(a) are plots of the absolute values of the storage and loss moduli multiplied by the MWCNT cross-sectional area versus the average sample displacement for the AFM-tipped MWCNT configuration whose behavior was illustrated in Figs. 2(a) and 3. We have plotted the in-phase and out-of-phase components of the measured force divided by the measured strain, which correspond to the storage and loss moduli multiplied by the cross-sectional area, instead of the moduli themselves.²¹ The determination of the actual cross-sectional area is complicated by the thickness of a CNT wall, the exact number of walls involved in bearing the axial load, etc., which we were unable to measure in this case. The inset shows the plot of the absolute value of the loss tangent ($\tan \delta$) versus the average sample displacement. The strain amplitude used at each average sample displacement is within the linear viscoelastic regime in each case ($< 4\%$ for the positive stiffness regime and $< 3\%$ for the negative stiffness regime). Note that the negative stiffness regime begins at an average sample displacement (strain) of ~ 200 nm ($\sim 17\%$) and ends at ~ 250 nm ($\sim 33\%$) here.

We observe marked increases in the absolute values of $\tan \delta$ and the two moduli after the buckling (kinking) transition at ~ 200 nm. A 400–600% increase in the absolute value of $\tan \delta$ is observed in the initial postbuckled (kinked) negative stiffness regime, and the increase remains large in the latter parts of the negative stiffness regime. $\tan \delta$ is negative for this regime as the phase angle between the force and sample displacement exceeds 90° ; hence, the absolute values in both regimes are shown instead. The loss modulus also has the same trend as the loss tangent before and right after kinking ($\sim 600\%$ increase right after kinking). The increase is less drastic as we progress further in the postbuckled regime. Likewise, the absolute value of the storage modulus increases right after kinking, but subsequently drops in the

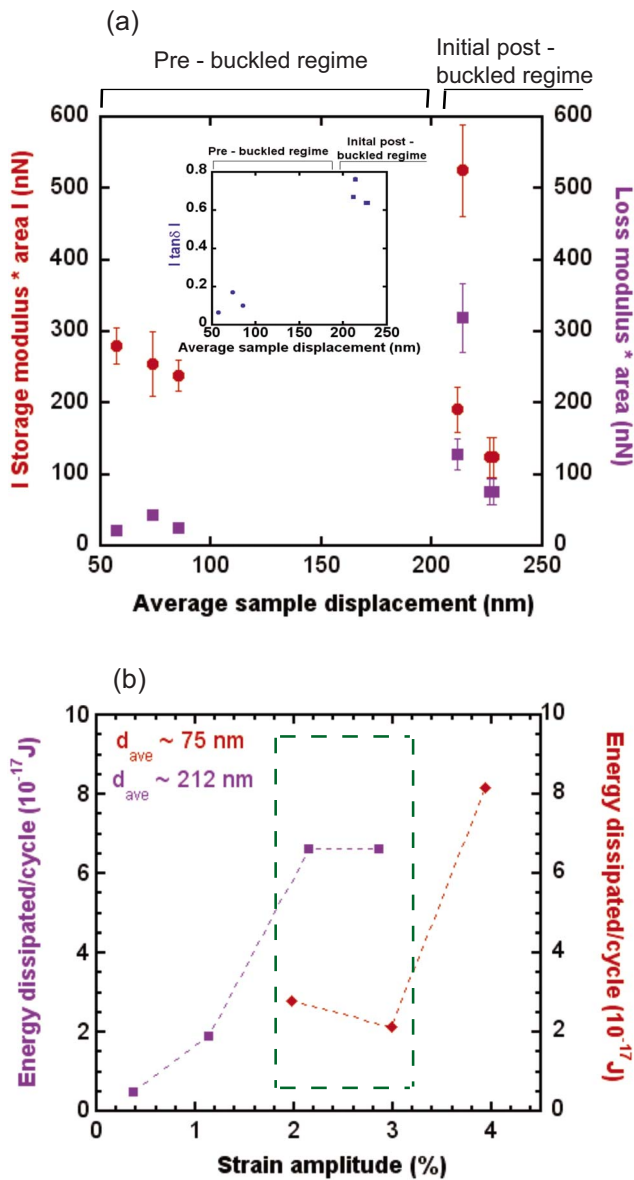


FIG. 4. (Color online) Linear viscoelastic properties of the AFM tip-mounted MWCNT (scheme I). (a) Absolute values of the storage and loss moduli (multiplied by the cross-sectional area) at different average sample displacements d_{av} in both prebuckled and initial postbuckled regimes. The inset shows the absolute value of $\tan \delta$ at different average sample displacements d_{av} . Marked increases in $\tan \delta$ and the moduli are observed immediately after buckling. (b) Energy dissipation per cycle at various strain amplitudes in both the prebuckled (brown) and initial postbuckled (purple) regimes. More energy is dissipated in the initial postbuckled negative stiffness regime than in the prebuckled positive stiffness regime at roughly the same strain amplitudes (green boxed region). Error bars are within the size of the symbols for certain data points.

later stages of the kinked regime, even to values below those in the prekinked regime. This result shows that in the kinked regime of the CNT, it is possible to achieve high overall stiffness and enhanced damping for this AFM-CNT configuration.

Figure 4(b) shows the energy dissipation per cycle at different linear strain amplitudes for both prekinked and initially postbuckled (kinked) regimes (at average sample displacements of ~ 75 and ~ 212 nm, respectively). The main source of energy dissipation in this system is the MWCNT itself, as the quality factors Q of AFM cantilevers are typically in the range of 50–300 in air. This remains the same whether the CNT is in the pre- or initially postkinked regime. Thus, any increase in dissipation after buckling is due to the kinked configuration of the CNT. In general, the energy dissipation per cycle increases as the strain amplitude increases. At these small strain amplitudes and in this positive stiffness regime where the CNT is almost straight or just slightly curved, the energy dissipated per cycle is minute, i.e., mid 10^{-17} J range. At strain amplitudes of 2–3 % [see boxed region in Fig. 4(b)], the amount of energy dissipated increases by 150–210 % in the negative stiffness regime (absolute increase of $\sim 6 \times 10^{-17}$ J).

The mechanism of increased dissipation in kinked MWCNTs is not well understood as of yet. It has been suggested by Ru²² that the walls cannot slip over each other easily in the vicinity of the kink because of the reduction in the interwall spacing, thus creating more internal friction and mechanical damping. Zheng *et al.*²³ obtained an expression for the average van der Waals interaction energy between a monolayer graphite sheet and a single carbon atom, $\Phi(s)$, spaced at the equilibrium normalized interwall or intershell distance s apart [Eq. (7) of Ref. 23]. This can be extended to the average van der Waals interaction energy between two walls of overlapping length x (nm), $U(x)$. In the case of kinking, this interaction energy in the kinked region is changed due to the reduced interwall spacing. The change in the average interaction energy, ΔU , is given by

$$\Delta U \approx 119.94 \times 10^{18} \Delta \Phi D x, \quad (1)$$

where $\Delta \Phi = \Phi(s') - \Phi(s)$, s' is the reduced normalized interwall spacing, and D (nm) is the inner wall diameter. The above analysis is, unfortunately, for a double walled CNT. No explicit analytical expression exists for the case of an N -walled MWCNT. We simply, to first approximation, multiply ΔU by $N/3$ (for considerably sized N -walled MWCNT, not all walls partake in the kinking, only the outer ones) to obtain the total change in the average interaction energy. D here is then the mean diameter of the walls that undergo kinking. Any quantitative calculation of the total change in interaction energy is further impeded by the uncertainty of the extent of the kinking. As the kinks are small localized regions as compared to the whole MWCNT and the strain amplitudes applied are tiny, we assume minute changes in interwall spacing ($s' = 2.3$) and overlapping lengths (30 nm). With these assumptions, we estimate that the increase in the average interaction energy for the AFM-tipped MWCNT is $\sim 10^{-16}$ J, which is close to the observed amount of energy dissipated. Thus, the slight increase in the van der Waals' interaction because of the kink is a plausible source of the increase in damping. Note that there is no mention of the change in bond energy. We assume that this is smaller in magnitude as compared to the change in van der Waals interaction energy.

Controlled uniaxial cyclic loading tests were also performed on AAO-grown MWCNTs/Fs using an AFM tip. Once again, reversible cycles of negative stiffness were observed. Figure 5(a) shows the absolute values of the storage and loss moduli multiplied by the MWCNT cross-sectional area (i.e., the in-phase and out-of-phase components of the force divided by the strain) plotted versus the average sample displacement for an AAO-grown MWCNT/F configuration [as shown in Fig. 2(b)]. The inset shows the plot of the absolute value of $\tan \delta$ versus the average sample displacement. The initial postbuckled regime spans only a few tens of nanometers in displacement, unlike that for the tip-mounted MWCNT [Fig. 2(a)]. As such, to stay within the bounds of linear viscoelasticity in this regime, uniaxial cyclic loading must be performed with rather small strain amplitudes, specifically $<1.2\%$ and $<0.65\%$ in the prebuckled and initial postbuckled negative stiffness regimes, respectively.

There is an increase of $\sim 145\%$ in the absolute value of $\tan \delta$, and $\sim 100\%$ and $\sim 330\%$ increases in absolute value of storage modulus and loss modulus (multiplied by cross-sectional area) respectively after buckling. Like the results for the tip-mounted MWCNT configuration, the behavior qualitatively follows the results for macroscopic tubes.⁴ However, in contrast with those results, enhanced overall stiffness (in absolute magnitude) is also observed. Figure 5(b) shows the dissipated energy per cycle at different strain amplitudes for both prebuckled and initial postbuckled regimes (at average sample displacements of ~ 22 and ~ 39 nm, respectively). If we extrapolate the strain amplitudes to 2–3 %, the energy dissipated per cycle would be in the 10^{-15} J range, almost 2 orders of magnitude more than those for the AFM tip-mounted MWCNT configuration. This may be due to the fact that the AAO-grown MWCNTs/Fs are thicker and taller, thus involving more wall-wall interactions and leading plausibly to more energy dissipation due to various reasons.

We also notice some energy dissipation in the prebuckled regime for the AFM tip on the AAO-grown MWCNT/F configuration. This is in contrast to the nearly unobservable energy dissipation in the prebuckled stages of the AFM tip-mounted MWCNT configuration. This difference is possibly attributed to the fact that the compression and buckling mechanisms are starkly different. Based on our previous measurements and consistent with MD simulations,⁹ we believe that even prior to symmetric shell buckling, considerable interwall sliding already occurs, hence mechanical dissipation. This was implicitly assumed in determining the critical buckling strains of these MWCNT/F previously.¹¹ In the tip-mounted MWCNT, there is little or almost no sliding between the walls prior to kinking. Instead, Euler buckling occurs, which involves the walls in the MWCNT bending collectively.

The percentage increase ($\sim 100\%$, absolute increase of $\sim 1.5 \times 10^{-16}$ J) witnessed in energy dissipation in the initial postbuckled negative stiffness regime for this configuration [see the boxed region in Fig. 5(b)] is less than that of the AFM tip-mounted MWCNT configuration (150–200 %). This may be explained by our hypothesis that the negative stiffness in this AAO-mounted MWCNT is associated with

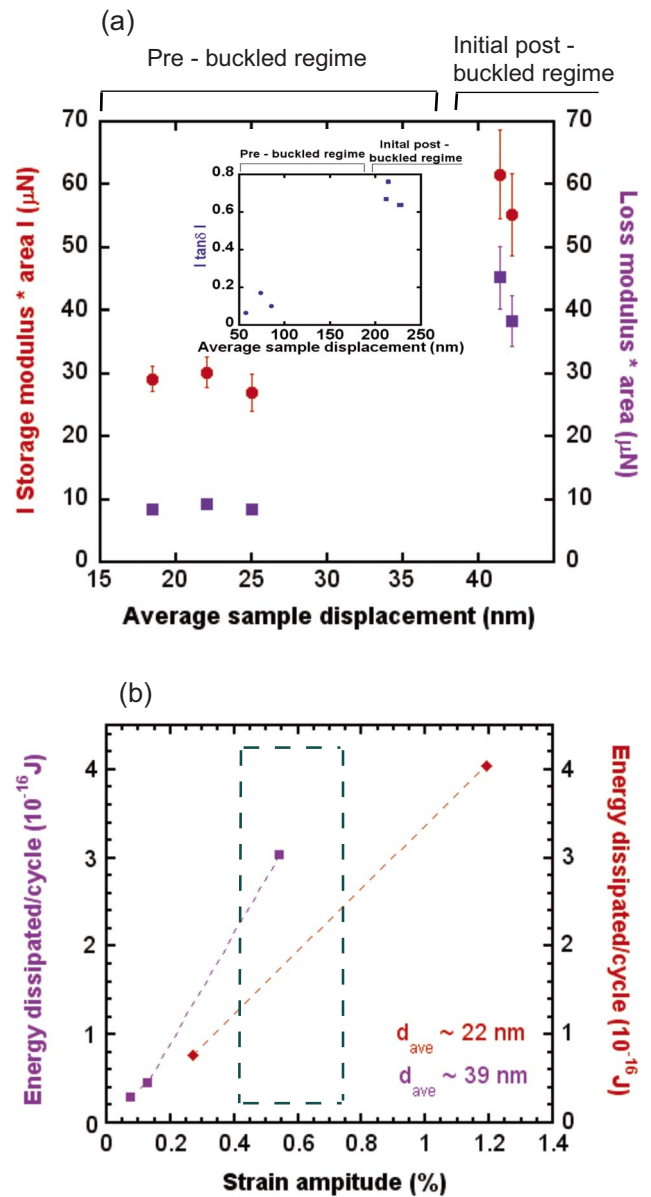


FIG. 5. (Color online) Viscoelastic properties of the AFM tip on an AAO-grown MWCNT/F (scheme II). (a) Absolute values of storage and loss moduli (multiplied by the cross-sectional area) at different displacements d_{av} in both prebuckled and initial postbuckled regimes. The inset shows the absolute value of $\tan \delta$ at different average sample displacements d_{av} . Once again, marked increases in $\tan \delta$ and moduli are observed immediately after buckling. (b) Energy dissipation per cycle at various strain amplitudes in both the prebuckled (brown) and initial postbuckled (purple) regimes. More energy is dissipated in the initial postbuckled negative stiffness regime than in the prebuckled positive stiffness regime at the same strain amplitudes (green boxed region). However, percentage increases are less than those for the AFM tip-mounted MWCNT. Error bars are all within the size of the symbols.

initial postsymmetric shell buckling and not kinking. In this regime, there is no localized transverse bending of the MWCNT, just wavelike distortions along the whole length of the tube. While there will exist localities along the tube that

will exhibit higher interwall stress and slightly reduced interwall spacing as a result of the distortions, there are also regions of reduced stress.⁹ Thus, the net change in van der Waals interaction between the walls is not as significant as those for a kinked CNT, and so the enhancement of mechanical damping after shell buckling for an AAO-grown MWCNT/F is not as drastic. Another possible reason is that there is only a marginal increase in interwall sliding in this initial postbuckled regime compared to the prebuckled regime.

For these MWCNTs, it is unlikely that our loading process can excite vibrational modes, which are in the gigahertz or terahertz range. A detailed study would have to take into consideration the presence of topological, intrinsic, and even volume defects. These would modulate the van der Waals interaction between the walls of a MWCNT/F and hence mechanical dissipation, though it has also been shown that certain defects do not hinder ultralow frictional sliding between walls.²⁴

IV. CONCLUSIONS

In summary, the viscoelastic properties of Reuss-like AFM-MWCNT/F mechanical configurations are investi-

gated. The sharp increase in the $\tan \delta$ in the initial postbuckled negative stiffness region replicates the trend seen in macroscopic tubes by Lakes.⁴ In addition, we find that asymmetric buckling (kinking), which occurs in longer aspect ratio MWCNTs/Fs, leads to larger energy dissipation than symmetric buckling. These ensembles cannot be exactly portrayed by the Reuss model since there are only a total of two components. However, the results lend credence to the concept of incorporating negative stiffness inclusions such as buckled MWCNTs/Fs into matrices to create nanocomposites with extreme mechanical properties such as enhanced damping and stiffness. Harnessing these properties will advance the field of nanocomposites and have far-reaching consequences in structural and mechanical systems.

ACKNOWLEDGMENTS

The authors acknowledge the financial support of NSF under Grant No. CMS-0136986. They thank Alex Kvit for expert assistance with the TEM. Correspondence and requests for materials should be addressed to R.W.C.

*carpick@seas.upenn.edu

- ¹R. S. Lakes, Phys. Rev. Lett. **86**, 2897 (2001).
- ²R. S. Lakes, T. Lee, A. Bersie, and Y. C. Wang, Nature (London) **410**, 565 (2001).
- ³T. Jaglinski, D. Kochmann, D. S. Stone, and R. S. Lakes, Science **315**, 620 (2007).
- ⁴R. S. Lakes, Philos. Mag. Lett. **81**, 95 (2001).
- ⁵N. Yamaki, *Elastic Stability of Circular Cylindrical Shells*, North-Holland Series in Applied Mathematics and Mechanics (North-Holland, Amsterdam, 1984).
- ⁶S. Iijima, C. Brabec, A. Maiti, and J. Bernholc, J. Chem. Phys. **104**, 2089 (1996).
- ⁷M. R. Falvo, G. J. Clary, R. M. Taylor, V. Chi, F. P. Brooks, S. Washburn, and R. Superfine, Nature (London) **389**, 582 (1997).
- ⁸B. I. Yakobson, C. J. Brabec, and J. Bernholc, Phys. Rev. Lett. **76**, 2511 (1996).
- ⁹A. Pantano, M. C. Boyce, and D. M. Parks, ASME J. Eng. Mater. Technol. **126**, 279 (2004).
- ¹⁰A. Garg, J. Han, and S. B. Sinnott, Phys. Rev. Lett. **81**, 2260 (1998).
- ¹¹H. W. Yap, R. S. Lakes, and R. W. Carpick, Nano Lett. **7**, 1149 (2007).
- ¹²N. Koratkar, B. Wei, and P. M. Ajayan, Adv. Mater. (Weinheim, Ger.) **14**, 997 (2002).
- ¹³J. Suhr, N. A. Koratkar, P. Koblinski, and P. M. Ajayan, Nat. Mater. **4**, 134 (2005).
- ¹⁴N. A. Koratkar, J. Shur, A. Joshi, R. S. Kane, L. S. Schadler, P. M. Ajayan, and S. Bartolucci, Appl. Phys. Lett. **87**, 063102 (2005).
- ¹⁵W. Zhang, J. Shur, and N. A. Koratkar, Adv. Mater. (Weinheim, Ger.) **18**, 452 (2006).
- ¹⁶J. Shur, W. Zhang, P. M. Ajayan, and N. A. Koratkar, Nano Lett. **6**, 219 (2006).
- ¹⁷These were purchased from Nanoscience Instruments, Inc., Arizona.
- ¹⁸H. Y. Yap, B. Ramaker, A. V. Sumant, and R. W. Carpick, Diamond Relat. Mater. **15**, 1622 (2006).
- ¹⁹R. S. Lakes, *Viscoelastic Solids*, CRC Mechanical Engineering Series (CRC, Baton Rouge, FL, 1998).
- ²⁰No frequency dependence was observed in the 1–5 Hz range.
- ²¹The product of the moduli and cross-sectional area is actually equal to the corresponding relevant forces divided by the maximum strain. These, in turn, can be obtained easily from hysteretic loops like those in Fig. 3. See Ref. 19 above for further details.
- ²²C. Q. Ru, J. Appl. Phys. **89**, 3426 (2001).
- ²³Q. Zheng, J. Z. Liu, and Q. Jiang, Phys. Rev. B **65**, 245409 (2002).
- ²⁴A. Kis, K. Jensen, S. Aloni, W. Mickelson, and A. Zettl, Phys. Rev. Lett. **97**, 025501 (2006).